Accuracy of Magnetic Field-based Train Localization and the Impact of Unknown Calibration Parameters

Benjamin Siebler, Stephan Sand, *German Aerospace Center (DLR)*
Uwe D. Hanebeck, *Karlsruhe Institute of Technology (KIT)*

BIOGRAPHY

Benjamin Siebler received his M.Sc. in electrical engineering and information technology from the KIT in 2014 and is currently pursuing his Ph.D. at the Intelligent Sensor-Actuator-Systems Laboratory of the KIT. Since 2014 he is a researcher at DLR with focus on multisensor localization with inertial sensors and magnetic field distortions.

Stephan Sand received his Ph.D. from ETH Zurich, Switzerland in 2010. Since 2002 Stephan has researched wireless communications and multi-sensor navigation at DLR. Since 2014 he is leading the Vehicular Applications Group and since 2024 he is leading the Communications Systems department researching robust navigation and wireless communications technologies for terrestrial and aerospace applications. Stephan has authored and co-authored more than 100 publications.

Uwe D. Hanebeck is full professor of Computer Science at KIT and director of the Intelligent Sensor-Actuator-Systems Laboratory (ISAS). He obtained his Ph.D. degree in 1997 and his habilitation degree in 2003, both in Electrical Engineering from the Technical University in Munich, Germany. His research interests are in information fusion, nonlinear state estimation, stochastic modeling, system identification, and control. He is author and coauthor of more than 600 publications and an IEEE Fellow.

ABSTRACT

The idea of magnetic field-based train localization is derived from the observation that magnetic material in the vicinity of railway tracks introduces position-specific and time-invariant distortions in the Earth magnetic field. A map of the magnetic field thus can be used to estimate the position of a train by comparing the map to the measurements of a train-mounted magnetometer.

In this paper, we derive and evaluate the Bayesian Cramér-Rao lower Bound (BCRLB) for magnetic field-based train localization with simultaneous magnetometer calibration. The BCRLB gives a lower limit for the achievable position accuracy and allows to systematically analyze the impact of unknown but jointly estimated calibration parameters. Furthermore, the bound can be used to show the observability of all calibration parameters.

I. INTRODUCTION

Rail transport is very efficient in terms of greenhouse gas emissions, especially compared to road transport [European Environment Agency, 2021]. In the face of climate change it is therefore desirable to shift traffic from the road to railways. To handle the additional traffic, the capacity of the existing railway network needs to be increased. Increasing the capacity by building new tracks is often not practical due high costs, long construction times or a lack of space, e.g., in dense urban areas. As an alternative, capacity can be increased by utilizing the existing track network more efficiently by introducing a higher degree of automation. Automation allows to reduce the safety distance between consecutive trains from the absolute braking distance to the relative braking distance. Furthermore, automation enables new operational concepts such as virtual coupling that is expected to increase the network capacity considerably. In a virtually coupled train set the different trains can split up on-the-fly since they are only coupled over a communication link and the distance between them is controlled automatically. For virtual coupling and automation in general, the locations of the trains in the network play a crucial role. Therefore, train localization is regarded as one of the core technologies in future railway systems and great efforts are made to establish global navigation satellite systems (GNSS) in the railway environment. These efforts will be successful for most areas of the railway network but there will be always areas in which the performance of GNSS is not sufficient due to shadowing and multi path propagation.

For a couple of years, we therefore advocate the use of distortions of the Earth magnetic field for train localization. The idea of magnetic field-based localization is derived from the observation that the Earth magnetic field along a railway track is strongly distorted by magnetic material in its vicinity. These distortions are characteristic for a certain position on the track and are persistent over time. Thus, the distortions can be seen as a magnetic fingerprint that can be used for train localization. Magnetic localization is a standalone technology, e.g., for tunnels, but can also serve as a redundant source of position information

when GNSS is available. The feasibility of magnetic localization was already shown for different environments, such as indoors [Haverinen and Kemppainen, 2009], road [Shockley and Raquet, 2014], and air [Canciani and Raquet, 2017]. For railways, the feasibility of magnetic localization was shown, e.g., in [Siebler et al., 2020].

In addition to showing the general feasibility for railways, we derived the BCRLB to analyze the theoretically achievable position accuracy in [Siebler et al., 2023b]. The bound in [Siebler et al., 2023b] considers only the case of a perfectly calibrated magnetometer. This assumption is rarely fulfilled in practice, as standard calibration methods require a rotation of the magnetometer and the platform it is mounted on in a homogeneous magnetic field. For a train-mounted sensor, this is not feasibly without considerable effort. Hence, we developed a simultaneous localization and calibration (SLAC) algorithm [Siebler et al., 2023a]. The key idea of SLAC is that when a train passes through a distorted magnetic field, the changes in the magnetic field not only allow localization, but also excite all magnetometer axes such that the calibration parameters become observable.

This paper now combines the BCRLB from [Siebler et al., 2023b] with the idea of SLAC. The newly derived bound allows to analyze the impact of the unknown calibration parameters on the position accuracy and shows how well the parameters can be estimated.

II. METHODOLOGY

The SLAC algorithm proposed in [Siebler et al., 2023a] jointly estimates the calibration parameters alongside the position. SLAC is based on Bayesian estimation principles and therefore a lower bound for SLAC also has to be Bayesian. In the following, we thus give a brief overview about the BCRLB and show how it can be calculated recursively. After a general introduction, the concrete equations for the SLAC BCRLB are derived. To show the impact of unknown parameters on the position accuracy, a second bound is derived that considers the parameters to be known random parameters.

1. Bayesian Cramér-Rao Lower Bound

The BCRLB is a bound on the the mean square error (MSE) matrix $\mathbf{M}$ and fulfills the matrix inequality

$$\mathbf{M} = \mathrm{E}_{\mathbf{x},\mathbf{z}}\left[(\hat{\mathbf{x}}(\mathbf{z}) - \mathbf{x})(\hat{\mathbf{x}}(\mathbf{z}) - \mathbf{x})^T\right] \geq \mathcal{J}^{-1} \,, \tag{1}$$

where $\mathcal{J}$ is the Bayesian information matrix (BIM), $\hat{\mathbf{x}}(\mathbf{z})$ is an estimator of the state $\mathbf{x}$ given the observations $\mathbf{z}$, and the expectation is calculated w.r.t. the joint probability density function (pdf) $p(\mathbf{z}, \mathbf{x})$ as indicated in the index. The inequality here means that the difference $\mathbf{M} - \mathcal{J}^{-1} \geq \mathbf{0}$ is a semi-positive definite matrix. The BIM was first introduced by Van Trees [Van Trees, 2004] and is given by

$$\mathcal{J} = -\mathrm{E}_{\mathbf{x},\mathbf{z}}\left[\Delta^{\mathbf{x}}_{\mathbf{x}} \ln\left(p(\mathbf{z}, \mathbf{x})\right)\right] \,. \tag{2}$$

In (2) the differential operator is the outer product of two nabla operators $\Delta^{\mathbf{a}}_{\mathbf{b}} = \nabla_{\mathbf{b}} \nabla^T_{\mathbf{a}}$. For brevity the regularity conditions of the BIM are omitted here, for the interested reader they can be found in the textbook [Van Trees, 2004]. The BIM is strongly connected to the Fisher information matrix (FIM) from the classical Cramér-Rao lower bound. The connection is easily revealed by substituting the joint density in (2) with $p(\mathbf{z}, \mathbf{x}) = p(\mathbf{z}|\mathbf{x})p(\mathbf{x})$ which yields

$$\begin{aligned}\mathcal{J} &= -\mathrm{E}_{\mathbf{x}}\left[\mathrm{E}_{\mathbf{z}|\mathbf{x}}\left[\Delta^{\mathbf{x}}_{\mathbf{x}} \ln\left(p(\mathbf{z}|\mathbf{x})p(\mathbf{x})\right)\right]\right] = \mathrm{E}_{\mathbf{x}}\left[-\mathrm{E}_{\mathbf{z}|\mathbf{x}}\left[\Delta^{\mathbf{x}}_{\mathbf{x}} \ln p(\mathbf{z}|\mathbf{x})\right]\right] + \mathrm{E}_{\mathbf{x}}\left[-\Delta^{\mathbf{x}}_{\mathbf{x}} \ln p(\mathbf{x})\right] \\ &= \mathrm{E}_{\mathbf{x}}\left[\mathcal{F}(\mathbf{x})\right] + \mathrm{E}_{\mathbf{x}}\left[-\Delta^{\mathbf{x}}_{\mathbf{x}} \ln p(\mathbf{x})\right] \,,\end{aligned} \tag{3}$$

with the FIM

$$\mathcal{F}(\mathbf{x}) = -\mathrm{E}_{\mathbf{z}|\mathbf{x}}\left[\Delta^{\mathbf{x}}_{\mathbf{x}} \ln p(\mathbf{z}|\mathbf{x})\right] \,. \tag{4}$$

In essence, the BIM is the sum of the information obtained from the observations, represented by the expected value of the FIM $\mathrm{E}_{\mathbf{x}}\left[\mathcal{F}(\mathbf{x})\right]$ over all possible states, and the information obtained from the prior distribution, which is the second term in (3).

2. Bound for Nonlinear Filtering

To find a bound for nonlinear filtering we have to account for changes in the state $\mathbf{x}$ over time. The BIM can account for time variant states by stacking the sate over multiple time steps into a single long vector of the form $\mathbf{x}_{0:k} = \begin{bmatrix}\mathbf{x}_0^\top & \cdots & \mathbf{x}_k^\top\end{bmatrix}^\top$, where the index indicates the time step. The BIM for the state sequence $\mathbf{x}_{0:k}$ can be directly obtained from (2)

$$\mathcal{J}_{0:k} = -\mathrm{E}_{\mathbf{x}_{0:k},\mathbf{z}_{1:k}}\left[\Delta^{\mathbf{x}_{0:k}}_{\mathbf{x}_{0:k}} \ln\left(p(\mathbf{z}_{1:k}, \mathbf{x}_{0:k})\right)\right] \,, \tag{5}$$

where $\mathbf{z}_{1:k}$ is the sequence of observations available at the time step k. However, the dimension of $\mathcal{J}_{0:k}$ is $((k+1)\cdot\dim(\mathbf{x}))\times((k+1)\cdot\dim(\mathbf{x}))$ and therefore increases with each new time step added to the sequence $\mathbf{x}_{0:k}$. Depending on the sequence length and the state dimension, this can lead to memory and complexity problems. In [Tichavsky et al., 1998], the authors propose a recursive version of the BCRLB where the involved matrices have a fixed dimension and do not depend on the length of the sequence. In order to apply the recursive version, the state space system that governs the time evolution of the state and the observation model must have the Markov property. Considering that most recursive filter algorithms also require the Markov property, this assumption is fulfilled in many practical applications. More details about the derivation of the recursive bound can be found in [Tichavsky et al., 1998] and [Siebler Access 2022]. For a Markovian system the BIM for each time step can be calculated from the BIM in the previous time step with the following recursion

$$\mathcal{J}_{k+1} = \mathbf{D}_k^{22} - (\mathbf{D}_k^{12})^T \left(\mathbf{D}_k^{11} + \mathcal{J}_k\right)^{-1} \mathbf{D}_k^{12} \,, \tag{6}$$

where the matrices $\mathbf{D}_k^{11}$, $\mathbf{D}_k^{12}$ and $\mathbf{D}_k^{22}$ are given by

$$\begin{aligned}
\mathbf{D}_k^{11} &= -\,\mathrm{E}_{\mathbf{x}_{k:k+1}}\left[\Delta_{\mathbf{x}_k}^{\mathbf{x}_k} \ln p(\mathbf{x}_{k+1}|\mathbf{x}_k)\right] \\
\mathbf{D}_k^{12} &= -\,\mathrm{E}_{\mathbf{x}_{k:k+1}}\left[\Delta_{\mathbf{x}_k}^{\mathbf{x}_{k+1}} \ln p(\mathbf{x}_{k+1}|\mathbf{x}_k)\right] \\
\mathbf{D}_k^{22} &= -\,\mathrm{E}_{\mathbf{x}_{k+1},\mathbf{z}_{k+1}}\left[\Delta_{\mathbf{x}_{k+1}}^{\mathbf{x}_{k+1}} \ln p(\mathbf{z}_{k+1}|\mathbf{x}_{k+1})\right] - \mathrm{E}_{\mathbf{X}_{k:k+1}}\left[\Delta_{\mathbf{x}_{k+1}}^{\mathbf{x}_{k+1}} \ln p(\mathbf{x}_{k+1}|\mathbf{x}_k)\right] .
\end{aligned} \tag{7}$$

Note, the first term of $\mathbf{D}_k^{22}$ can be reformulated in terms of the expected FIM

$$\mathbf{D}_k^{22} = \mathrm{E}_{\mathbf{x}_{k+1}}[\mathcal{F}(\mathbf{x}_{k+1})] - \mathrm{E}_{\mathbf{X}_{k:k+1}}\left[\Delta_{\mathbf{x}_{k+1}}^{\mathbf{x}_{k+1}} \ln p(\mathbf{x}_{k+1}|\mathbf{x}_k)\right] \,. \tag{8}$$

So far these equations are rather generic and abstract. To make things more concrete, the next section defines the state space model governing the temporal behavior of the state $\mathbf{x}$ for which the bound is derived.

3. State Space Model for SLAC

The state space model consists of two parts, the motion model that describes how the state vector evolves from one time step to the next and an observation model that tells us how an observation is connected to the state. In this paper, the state vector $\mathbf{x}_k$ consists of two parts

$$\mathbf{x}_k = \begin{bmatrix}\mathbf{d}_k^\top & \boldsymbol{\theta}_k^\top\end{bmatrix}^\top \,, \tag{9}$$

where the dynamic state $\mathbf{d}_k \in \mathbb{R}^2$ contains the along-track position s_k and the speed $\dot{s}_k$ of the train

$$\mathbf{d}_k = \begin{bmatrix}s_k & \dot{s}_k\end{bmatrix}^\top \,. \tag{10}$$

The along-track position is a one-dimensional value that describes the position of the train on a known track and is limited to the interval $s_k \in [0, L_{\text{track}}]$ where L_{track} is the length of the track. The remainder of the state is the vector $\boldsymbol{\theta}_k$ containing the magnetometer calibration parameters that will be described in the end of the section. The dynamic model used throughout the paper is a simple linear model with an acceleration input

$$\begin{aligned}
\mathbf{x}_k = \begin{bmatrix}\mathbf{d}_k \\ \boldsymbol{\theta}_k\end{bmatrix} &= \begin{bmatrix}\mathbf{F}_\mathbf{d} & \mathbf{0}_{2\times 12} \\ \mathbf{0}_{12\times 2} & \mathbf{I}_{12\times 12}\end{bmatrix}\begin{bmatrix}\mathbf{d}_{k-1} \\ \boldsymbol{\theta}_{k-1}\end{bmatrix} + \begin{bmatrix}\mathbf{B}_\mathbf{d} \\ \mathbf{0}_{12\times 1}\end{bmatrix} a_{k-1} + \begin{bmatrix}\mathbf{I}_{2\times 2} \\ \mathbf{0}_{12\times 2}\end{bmatrix}\mathbf{w}_{k-1} \\
&= \mathbf{F}\mathbf{x}_{k-1} + \mathbf{B}a_{k-1} + \mathbf{G}\mathbf{w}_{k-1} \,,
\end{aligned} \tag{11}$$

with the system matrix $\mathbf{F}_\mathbf{d}$ and input matrix $\mathbf{B}_\mathbf{d}$

$$\mathbf{F}_\mathbf{d} = \begin{bmatrix}1 & T \\ 0 & 1\end{bmatrix}, \quad \mathbf{B}_\mathbf{d} = \begin{bmatrix}\frac{1}{2}T^2 \\ T\end{bmatrix} \,. \tag{12}$$

The process noise is Gaussian $\mathbf{w} \sim \mathcal{N}(\mathbf{0}, \mathbf{Q})$ with a covariance according to a continuous white noise acceleration model, cf. [Bar-Shalom et al., 2001],

$$\mathbf{Q} = \begin{bmatrix}\frac{1}{3}T^3 & \frac{1}{2}T^2 \\ \frac{1}{2}T^2 & T\end{bmatrix}\tilde{q} \,, \tag{13}$$

where T is the duration between two consecutive time steps. The system matrix of the calibrations parameters $\boldsymbol{\theta}_k$ in (11) is the identity matrix $\mathbf{I}$ and the parameters are unaffected by the acceleration input and the process noise. The parameters are therefore modeled as unknown but perfectly constant. This might not be practical in the implementation of a filter but in a bound this causes no problems. To account for slowly changing parameters one can simply add a small process noise to the parameters.

The bound solely uses the observations of a vector magnetometer with three orthogonal axes. Furthermore, the magnetometer is assumed to be uncalibrated. With these assumptions the observation model becomes

$$\mathbf{z}_k = \mathbf{C}\,\mathbf{m}(s_k) + \mathbf{b} + \mathbf{n}_k \,, \tag{14}$$

where $\mathbf{m}(\cdot) : [0, L_{\text{track}}] \mapsto \mathbb{R}^3$ is a map of the magnetic field that maps the along-track position s_k to the magnetic vector field at that position and $\mathbf{n}_k \sim \mathcal{N}(\mathbf{0}_{3\times1}, \sigma_n^2\mathbf{I}_{3\times3})$ is the sensor noise. The calibration matrix $\mathbf{C} \in \mathbb{R}^{3\times3}$ and the bias vector $\mathbf{b} \in \mathbb{R}^3$ account for imperfections in the magnetometer caused by the hardware of the sensor, and soft and hard iron effects caused by the train on which the sensor is mounted. More details about the calibration model and the source of the imperfections can be found in [Renaudin et al., 2010, Kok and Schön, 2016]. Note, in the above model the magnetic map does not have to be created with a calibrated magnetometer. If the map was created with an uncalibrated magnetometer, $\mathbf{C}$ and $\mathbf{b}$ have to be understood as relative calibration parameters between two magnetometers. In [Siebler et al., 2023a] the requirements for the relative calibration are explained in detail and it is shown that in the railway domain the requirements are roughly met. In our previous work about SLAC we have shown that (14) can be reformulated in terms of a single parameter vector $\boldsymbol{\theta} \in \mathbb{R}^{12}$

$$\mathbf{z}_k = \mathbf{H}(s_k)\boldsymbol{\theta}_k + \mathbf{n}_k \,, \tag{15}$$

where $\mathbf{H}(s_k)$ is a matrix valued function

$$\mathbf{H}(s_k) = \begin{bmatrix} \begin{bmatrix}\mathbf{m}(s_k)^T & 1\end{bmatrix} & \mathbf{0}_{1\times4} & \mathbf{0}_{1\times4} \\ \mathbf{0}_{1\times4} & \begin{bmatrix}\mathbf{m}(s_k)^T & 1\end{bmatrix} & \mathbf{0}_{1\times4} \\ \mathbf{0}_{1\times4} & \mathbf{0}_{1\times4} & \begin{bmatrix}\mathbf{m}(s_k)^T & 1\end{bmatrix} \end{bmatrix} = \begin{bmatrix} \mathbf{h}_1^\top(s_k) \\ \mathbf{h}_2^\top(s_k) \\ \mathbf{h}_3^\top(s_k) \end{bmatrix} . \tag{16}$$

The parameter vector is composed of the rows from the calibration matrix $\mathbf{C}$ and the elements of the bias vector $\mathbf{b}$

$$\boldsymbol{\theta} = \begin{bmatrix}\mathbf{c}_1^\top & b_1 & \mathbf{c}_2^\top & b_2 & \mathbf{c}_3^\top & b_3\end{bmatrix}^\top . \tag{17}$$

Regarding the notation, the i-th row of $\mathbf{C}$ is represented by a column vector $\mathbf{c}_i$. This might be a bit confusing but avoids that we have to differentiate between column and row vectors in the remainder of the paper.

The reformulated observations model (15) shows that for a known train position the estimation of the calibration parameters is a linear estimation problem that can be solved efficiently with a linear estimator, e.g., a Kalman filter. The conditional linearity of the calibration parameters is also the basis for the Rao-Blackwellized particle filter used in SLAC. The Rao-Blackwellized filter has for each particle a separate Kalman filter which has two benefits. First, the states related to the parameters do not have to be sampled and thus the state space of the particle filter is kept small. Second, for each particle the parameters are estimated optimally by the Kalman filter. As the reminder of the paper will show, this decomposition of the estimation problem in a nonlinear and linear part also translates to the BCRLB such that the parts related to the calibration parameters can be calculated analytically and no numerical integration is required.

4. BCRLB for SLAC

The equations for the BCRLB and the state space model provide all the ingredients required for deriving the SLAC bound. The matrices $\mathbf{D}_k^{11}$, $\mathbf{D}_k^{12}$ and the second term of $\mathbf{D}_k^{22}$ in (7) are obtained in a straightforward way from the derivatives of $\ln p(\mathbf{x}_{k+1}|\mathbf{x}_k)$ due to the linearity of (11) w.r.t. the state

$$\begin{aligned} \mathbf{D}_k^{11} &= \mathbf{F}^\top(\mathbf{G}\mathbf{Q}\mathbf{G}^\top)^{-1}\mathbf{F} \\ \mathbf{D}_k^{12} &= -\mathbf{F}^\top(\mathbf{G}\mathbf{Q}\mathbf{G}^\top)^{-1} \\ \mathbf{D}_k^{22} &= \mathrm{E}_{\mathbf{x}_{k+1}}\left[\mathcal{F}(\mathbf{x}_{k+1})\right] + (\mathbf{G}\mathbf{Q}\mathbf{G}^\top)^{-1} . \end{aligned} \tag{18}$$

Inserting the above equations into (6) and using the Woodbury matrix identity yields a compact representation of $\mathcal{J}_{k+1}$

$$\mathcal{J}_{k+1} = \mathrm{E}_{\mathbf{x}_{k+1}}\left[\mathcal{F}(\mathbf{x}_{k+1})\right] + (\mathbf{G}\mathbf{Q}\mathbf{G}^\top + \mathbf{F}\mathcal{J}_k^{-1}\mathbf{F}^\top)^{-1} . \tag{19}$$

In the sequel, we derive the expected FIM in (19). For the FIM we first derive the likelihood from the observations model

$$p(\mathbf{z}_{k+1}|\mathbf{x}_{k+1}) = \mathcal{N}\left(\mathbf{z}_{k+1}; \mathbf{H}(s_{k+1})\boldsymbol{\theta}_{k+1}, \sigma_n^2 \mathbf{I}_{3\times 3}\right) \tag{20}$$

and, second insert it into the definition (4) of the FIM. For the derivation it is beneficial to divide the differential operator $\Delta_{\mathbf{x}_{k+1}}^{\mathbf{x}_{k+1}}$ into four blocks that reflect the structure of the state vector in (9)

$$\Delta_{\mathbf{x}_{k+1}}^{\mathbf{x}_{k+1}} = \begin{bmatrix} \nabla_{\mathbf{d}_{k+1}} \\ \nabla_{\boldsymbol{\theta}_{k+1}} \end{bmatrix} \begin{bmatrix} \nabla_{\mathbf{d}_{k+1}}^\top & \nabla_{\boldsymbol{\theta}_{k+1}}^\top \end{bmatrix} = \begin{bmatrix} \Delta_{\mathbf{d}_{k+1}}^{\mathbf{d}_{k+1}} & \Delta_{\mathbf{d}_{k+1}}^{\boldsymbol{\theta}_{k+1}} \\ \Delta_{\boldsymbol{\theta}_{k+1}}^{\mathbf{d}_{k+1}} & \Delta_{\boldsymbol{\theta}_{k+1}}^{\boldsymbol{\theta}_{k+1}} \end{bmatrix} . \tag{21}$$

Applying (21) to the likelihood yields a FIM in block form

$$\mathcal{F}(\mathbf{x}_{k+1}) = \frac{1}{\sigma_n^2} \begin{bmatrix} \mathbf{J}_\mathbf{H}(s_{k+1}) \left[\mathbf{I}_{3\times 3} \otimes \boldsymbol{\theta}_{k+1}\right] \left[\mathbf{I}_{3\times 3} \otimes \boldsymbol{\theta}_{k+1}\right]^\top \mathbf{J}_\mathbf{H}(s_{k+1})^\top & \mathbf{J}_\mathbf{H}(s_{k+1}) \left[\mathbf{I}_{3\times 3} \otimes \boldsymbol{\theta}_{k+1}\right] \mathbf{H}(s_{k+1}) \\ \left(\mathbf{J}_\mathbf{H}(s_{k+1}) \left[\mathbf{I}_{3\times 3} \otimes \boldsymbol{\theta}_{k+1}\right] \mathbf{H}(s_{k+1})\right)^\top & \mathbf{H}(s_{k+1})^\top \mathbf{H}(s_{k+1}) \end{bmatrix} , \tag{22}$$

where the Jacobian matrix $\mathbf{J}_\mathbf{H}$ is given by the derivatives of $\mathbf{H}(\cdot)$ w.r.t. the dynamic state

$$\mathbf{J}_\mathbf{H}(s_{k+1}) = \begin{bmatrix} \nabla_{\mathbf{d}_{k+1}} \mathbf{h}_1^\top(s_{k+1}) & \nabla_{\mathbf{d}_{k+1}} \mathbf{h}_2^\top(s_{k+1}) & \nabla_{\mathbf{d}_{k+1}} \mathbf{h}_3^\top(s_{k+1}) \end{bmatrix} . \tag{23}$$

For the BIM the expectation of the FIM over the pdf $p(\mathbf{x}_{k+1})$ is required. As it turns out, the expectation over the parameters $\boldsymbol{\theta}_{k+1}$ is easily calculated analytically such that only the expectation over $\mathbf{d}_{k+1}$ needs to be numerically integrated

$$\mathrm{E}_{\mathbf{x}_{k+1}}\left[\mathcal{F}(\mathbf{x}_{k+1})\right] = \frac{1}{\sigma_n^2} \mathrm{E}_{\mathbf{d}_{k+1}} \left[\begin{bmatrix} \mathbf{J}_\mathbf{H}(s_{k+1}) \left[\mathbf{I}_{3\times 3} \otimes \left(\boldsymbol{\mu}_{\boldsymbol{\theta}_{k+1}} \boldsymbol{\mu}_{\boldsymbol{\theta}_{k+1}}^\top + \boldsymbol{\Sigma}_{\boldsymbol{\theta}_{k+1}}\right)\right] \mathbf{J}_\mathbf{H}(s_{k+1})^\top & \mathbf{J}_\mathbf{H}(s_{k+1}) \left[\mathbf{I}_{3\times 3} \otimes \boldsymbol{\mu}_{\boldsymbol{\theta}_{k+1}}\right] \mathbf{H}(s_{k+1}) \\ \left(\mathbf{J}_\mathbf{H}(s_{k+1}) \left[\mathbf{I}_{3\times 3} \otimes \boldsymbol{\mu}_{\boldsymbol{\theta}_{k+1}}\right] \mathbf{H}(s_{k+1})\right)^\top & \mathbf{H}(s_{k+1})^\top \mathbf{H}(s_{k+1}) \end{bmatrix} \right] . \tag{24}$$

In (24) the vector $\boldsymbol{\mu}_{\boldsymbol{\theta}_{k+1}}$ is the predicted mean and $\boldsymbol{\Sigma}_{\boldsymbol{\theta}_{k+1}}$ the predicted covariance of the parameters vector at time step $k+1$. The predicted values are obtained by applying the system model to the Gaussian prior of the parameters $p(\boldsymbol{\theta}_0) = \mathcal{N}(\boldsymbol{\theta}_0; \boldsymbol{\mu}_{\boldsymbol{\theta}_0}, \boldsymbol{\Sigma}_{\boldsymbol{\theta}_0})$. Since the parameters are constant in the system model, the prediction is not necessary and $p(\boldsymbol{\theta}_{k+1}) = \mathcal{N}(\boldsymbol{\theta}_{k+1}; \boldsymbol{\mu}_{\boldsymbol{\theta}_0}, \boldsymbol{\Sigma}_{\boldsymbol{\theta}_0})$.

The magnetic map in the observation model is usually unknown analytically due to the complex interactions of the environment with the Earth magnetic field. Thus, the map has to be constructed from a set of observations. In [Siebler et al., 2023b] the map is represented by a Gaussian process (GP). Here, the GP will be used once more but in a simplified manner and the position dependent variance of the GP is not considered. This simplification is done because it gives rise to the above given compact bound in which the expectation of the parameters is performed analytically. Furthermore, including the position dependent variance of the GP might mask the impact of the unknown calibration parameters on the position accuracy.

5. BCRLB for Know Calibration Parameters

To see how the simultaneous estimation of the calibration parameters impact the position accuracy, the SLAC bound is compared against a second bound that assumes the parameters are still a random variable but this time their values are known during estimation. In other words, the state vector of the second bound only contains the dynamic state $\mathbf{d}_k$ but not the parameters. For a fair comparison, the expectation of the second bound over the prior distribution of the calibration parameters is calculated. Thus, the second bound is given by the inverse of the expected BIM

$$\mathcal{J}_{0:k}^{\boldsymbol{\theta}} = \mathrm{E}_{\boldsymbol{\theta}} \left[-\mathrm{E}_{\mathbf{d}_{0:k}, \mathbf{z}_{1:k}} \left[\Delta_{\mathbf{d}_{0:k}}^{\mathbf{d}_{0:k}} \ln\left(p(\mathbf{z}_{1:k}, \mathbf{d}_{0:k}; \boldsymbol{\theta})\right) \right] \right] , \tag{25}$$

where $\boldsymbol{\theta}$ is no longer part of the state but a parameter that changes the likelihood model (20) and thus the FIM derived from it. The calculation of (25) is closely related to the SLAC bound, but in the FIM only the position dependent part is accounted for and the system model in (11) is reduced to the parts that are related to the dynamic state. Similar to the SLAC bound, the BIM can be calculated in a recursive manner

$$\mathcal{J}_{k+1}^{\boldsymbol{\theta}} = \mathrm{E}_{\boldsymbol{\theta}} \left[\mathrm{E}_{\mathbf{d}_{k+1}} \left[\mathcal{F}(\mathbf{d}_{k+1}; \boldsymbol{\theta}) \right] \right] + \left(\mathbf{Q} + \mathbf{F}_\mathbf{d} (\mathcal{J}_k^{\boldsymbol{\theta}})^{-1} \mathbf{F}_\mathbf{d}^\top\right)^{-1} . \tag{26}$$

As before, the expectation of the FIM w.r.t. the parameters in $\mathrm{E}_{\boldsymbol{\theta}} \left[\mathrm{E}_{\mathbf{d}_{k+1}} \left[\mathcal{F}(\mathbf{d}_{k+1}; \boldsymbol{\theta}) \right] \right]$ can be calculated in closed form and is given by the upper left block of (24).

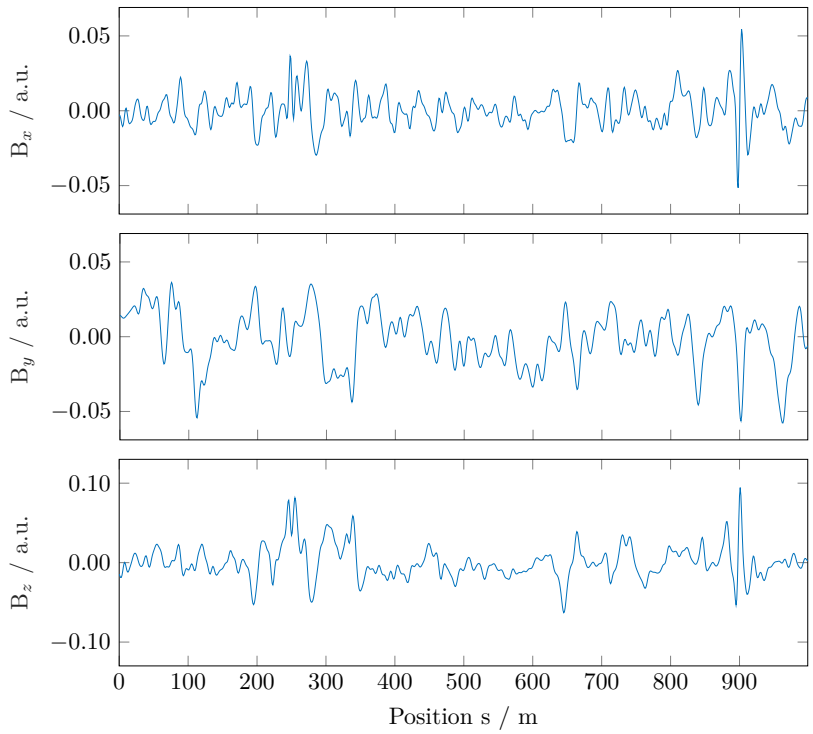

Figure 1: Mean of the GPs that represent the magnetic field map. Each component of the magnetic map is represented by a separate GP. The flux density in the graphs is dimensionless (a.u. stands for arbitrary units). This is because the magnetometer used for the measurements returns normalized data only. According to the data-sheet 1 a.u. correspond to $\approx 40\,\mu\mathrm{T}$.

III. EVALUATION

1. Measurement Setup and Map Generation

The proposed bounds are evaluated with the same data set and GP that was already used in [Siebler et al., 2023b]. The data for the GP training was recorded with a Alstom Coradia LINT 41 diesel-powered train from the Bayerische Regiobahn driving between Augsburg and Ingolstadt. The magnetic vector field was recorded with a Xsens MTi nine degree of freedom inertial measurement unit (IMU) at a frequency of $200\,\mathrm{Hz}$. The position of the IMU was obtained with a u-blox LEA-6T GPS receiver. The GP that represents the magnetic map in the bound covers a $1\,\mathrm{km}$ long track segment. The three components of the magnetic vector field are represented by three separate GPs. To get an impression of the magnetic field, the mean of the three GPs is shown in Fig. 1. More details about the training of the GP, its hyperparameters, and the equations for the derivative of the mean are described in [Siebler et al., 2023b].

2. Simulation Setup

For the results in the next section we use 1000 trajectories for the train position and train speed generated randomly from the system model (11). The random trajectories are then used to get an approximation of the expected value of the FIM in (19). Since the expectation over the parameters can be calculated in closed form, it is not necessary to sample the parameter space. Note, this is also true when the parameters are changing over time. In the generation of the position and speed trajectories we use a step width of $T = 0.1\,\mathrm{s}$ and an acceleration noise density of $0.0625\,\mathrm{m}^2/\mathrm{s}^3$. In total each trajectory is 300 time steps long. In the first 100 steps the acceleration input is set $2\,\mathrm{m\,s}^{-2}$, followed by 100 steps of zero acceleration then the acceleration is set to $-2\,\mathrm{m\,s}^{-2}$. The mean and covariance of the Gaussian prior of the dynamic state are set to $\boldsymbol{\mu}_{\mathbf{d}_0} = \begin{bmatrix}100\,\mathrm{m} & 5\,\mathrm{m\,s}^{-1}\end{bmatrix}^\top$ and $\boldsymbol{\Sigma}_{\mathbf{d}_0} = \mathrm{diag}(\begin{bmatrix}100\,\mathrm{m}^2 & 1\,\mathrm{m}^2\,\mathrm{s}^{-2}\end{bmatrix})$. The distribution of the trajectories generated from the above defined parameters is shown in Fig. 2. For the likelihood the standard deviation of the magnetometer sensor noise is set to $\sigma_n = 0.0037$, which was obtained from the GP hyperparameter optimization.

The mean and covariance of the Gaussian prior distribution $p(\boldsymbol{\theta}_0)$ of the calibration parameters $\boldsymbol{\theta}$ are set to different values during the evaluation. The changes in the prior focus on the calibration matrix $\mathbf{C}$, since changes in the prior of the bias have shown only little impact on the resulting bound. This is because the bias related parts in the Jacobian (23) are zero which renders

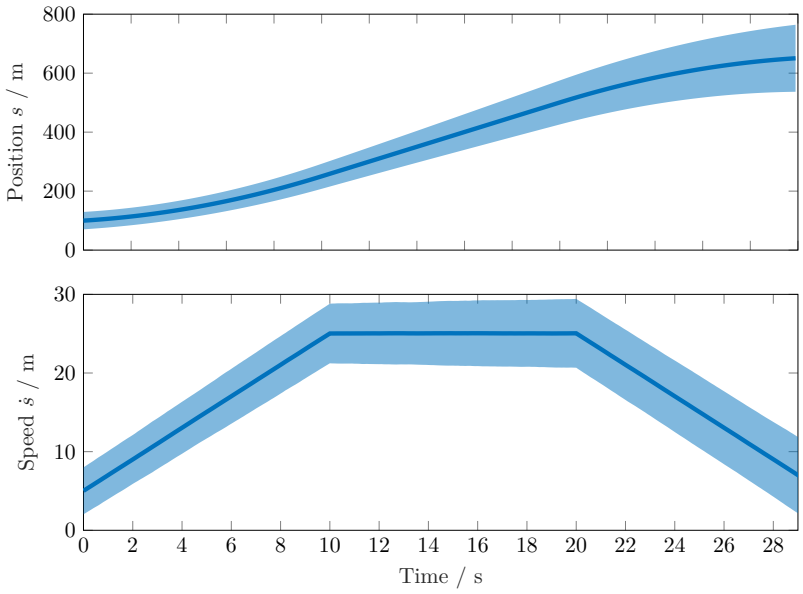

Figure 2: Position and speed distribution over the 300 time steps. The blue line shows the mean and the blue shaded area indicates three times the standard deviation. The mean value clearly shows the acceleration in the beginning and the deceleration towards the end.

the upper left block of the FIM independent from the bias. For the covariance we assume it is diagonal

$$\boldsymbol{\Sigma}_{\boldsymbol{\theta}_0} = \operatorname{diag}\left(\left[\sigma^2_{\mathbf{C}_{11}} \quad \sigma^2_{\mathbf{C}_{ij}} \quad \sigma^2_{\mathbf{C}_{ij}} \quad \sigma^2_{\mathbf{b}} \quad \sigma^2_{\mathbf{C}_{ij}} \quad \sigma^2_{\mathbf{C}_{22}} \quad \sigma^2_{\mathbf{C}_{ij}} \quad \sigma^2_{\mathbf{b}} \quad \sigma^2_{\mathbf{C}_{ij}} \quad \sigma^2_{\mathbf{C}_{ij}} \quad \sigma^2_{\mathbf{C}_{33}} \quad \sigma^2_{\mathbf{b}}\right]\right) , \tag{27}$$

and that all off-diagonal values of $\mathbf{C}$ and all bias components have each the same prior. The variance related to the three bias components is set to $\sigma_{\mathbf{b}} = 0.25$ and the mean is set to zero. The variance and the bias related to the off-diagonal elements in $\mathbf{C}$ are set to a fixed value of $\sigma_{\mathbf{C}_{ij}} = 0.05$ and $\mu_{\mathbf{C}_{ij}} = 0$. The only part of the prior that will be changed in the evaluation is the part related to the main diagonal elements of $\mathbf{C}$. We decided to fix all other parts of the prior because we want to focus on the parts that have a strong effect on the bound. Furthermore, we expect that changes in the distribution of the off-diagonal elements have a similar effect than changes in the main diagonal.

3. Results

In Fig. 3 we see the position BCRLB for SLAC $[\mathcal{J}^{-1}]_{11}$ and for known parameters $[(\mathcal{J}^{\boldsymbol{\theta}})^{-1}]_{11}$. The bounds are obtained for a fixed standard deviation of $\sigma_{\mathbf{C}_{ii}} = 0.05, i \in \{1, 2, 3\}$ and three different values for the mean $\mu_{\mathbf{C}_{11}}$ of the first diagonal element. The mean of the remaining elements is set to $\mu_{\mathbf{C}_{22}} = \mu_{\mathbf{C}_{33}} = 1$. For all three values of the mean $\mu_{\mathbf{C}_{11}}$ the two bounds are rather close to each other. This can be seen also from their ratios which show that the difference is in the range of just a few percent. Therefore, from a theoretic point of view using SLAC does not strongly affect the achievable position accuracy. However, one should keep in mind that the bound might not be attainable by an actual position estimator. Additionally, performing SLAC certainly increases the computational complexity of the magnetic localization system and thus hardware or runtime restrictions might lead to additional decreases in the position accuracy.

Besides the relative difference between the SLAC and known parameter bound, Fig. 3 also shows that the absolute values of the bounds for different mean values change considerable. This was to be expected from the equations of the bound in (24) and is also somewhat intuitive when we consider that a high absolute mean value for the elements in matrix $\mathbf{C}$ causes more likely an amplification of the values in the magnetic map. The amplification in combination with a constant sensor noise level results in an effective increase in the signal-to-noise ratio and therefore a lower positioning bound.

Similar to changes in the mean of the prior distribution, changes in the prior covariance strongly affect the resulting bounds. To investigate the sensitivity of the bound w.r.t. the covariance, Fig. 4 shows the bound for three different values of $\sigma_{\mathbf{C}_{11}}$ and a fixed mean $\mu_{\mathbf{C}_{11}} = 1$. For the other diagonal elements the prior stays the same, thus $\sigma_{\mathbf{C}_{ii}} = 0.05$ and $\mu_{\mathbf{C}_{ii}} = 1$ for $i \in \{2, 3\}$. As for the mean, there is a clear trend in the position bound, a higher covariance leads to an higher position accuracy. In contrast to a higher mean value, a higher variance seems to considerably lower the ratio between the two bounds, e.g., for $\sigma_{\mathbf{C}_{11}} = 5$ the ratio is close to one. This difference in the behavior compared to a high mean value can be explained by the structure of the FIM in (24). The variance only affects the upper left block related to the position. The mean on the other hand, also affects the

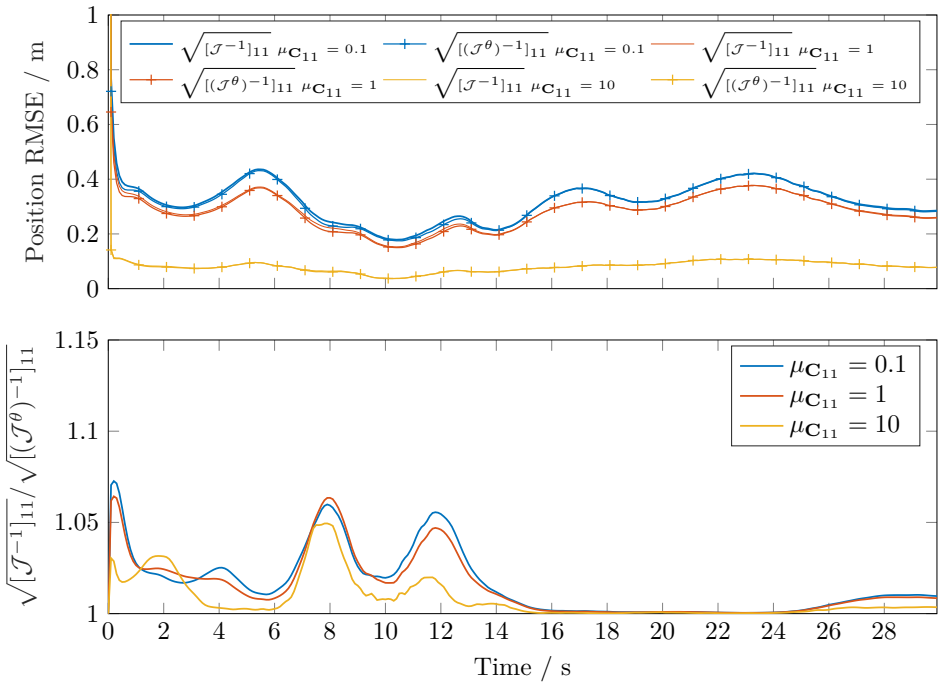

Figure 3: Position BCRLB for SLAC and known parameters for three different value of $\mu_{\mathbf{C}_{11}}$. (top) Absolute value of the square root of the position bounds. (bottom) Ratio between the SLAC and known parameter position bound.

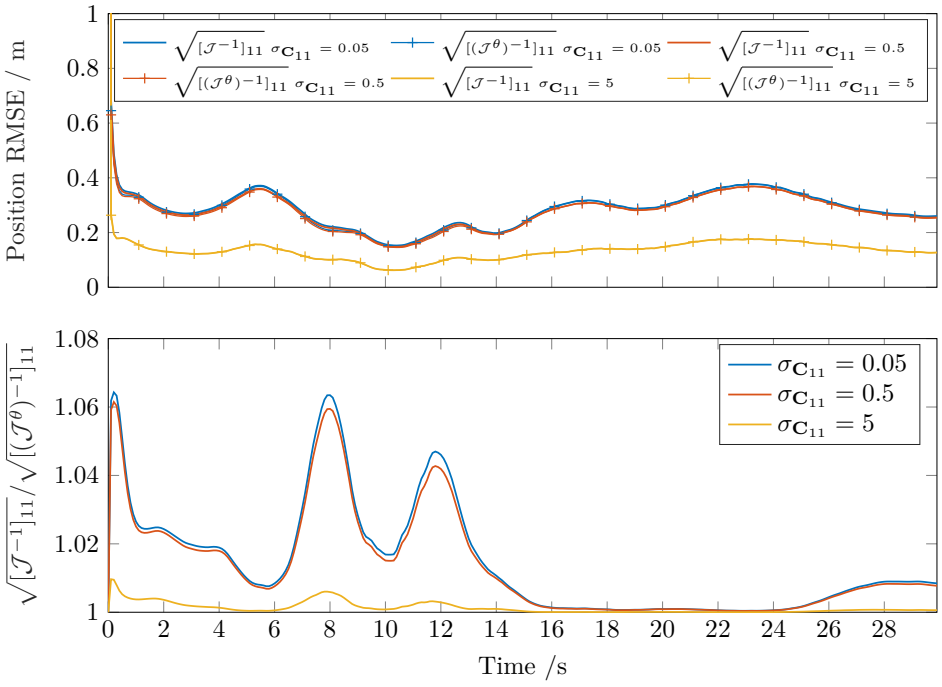

Figure 4: Position BCRLB for SLAC and known parameters for three different value of $\sigma_{\mathbf{C}_{11}}$. (top) Absolute value of the square root of the position bounds. (bottom) Ratio between the SLAC and known parameter position bound.

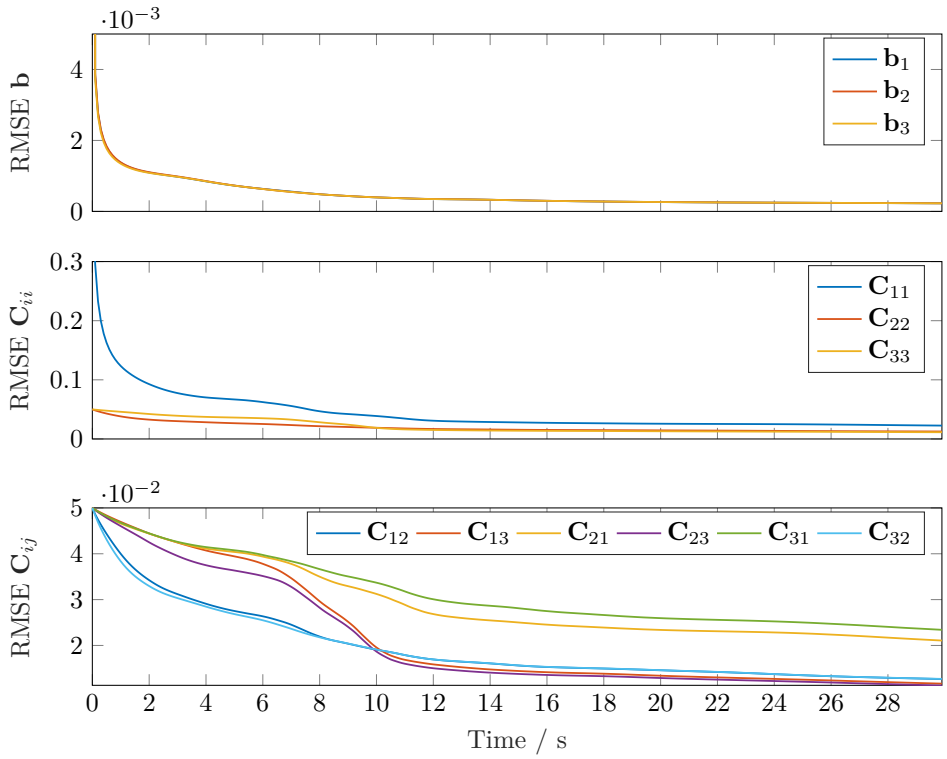

Figure 5: Parameter BCRLB for SLAC. (top) Square root of the bound related to the bias vector $\mathbf{b}$. (middle) Square root of the bound related to the main diagonal elements of $\mathbf{C}$. (bottom) Square root of the bound related to the off-diagonal elements of $\mathbf{C}$.

lower left and upper right block of the FIM, which represents the correlation between the parameters and the position.

The SLAC bound does not only provide the lower bound for the position, but also the bound for the parameter estimation. This is of particular interest because this part of the bound allows us to draw conclusions about the observability of the calibration parameters. In Fig. 5, the bounds for the parameters for $\mu_{\mathbf{C}_{11}} = 1$ and $\sigma_{\mathbf{C}_{11}} = 0.5$ is shown. For each of the twelve parameters the bound gets smaller over time and gets flat towards the end potentially converging to a steady state. Since this is true for all parameters, the bound suggests that SLAC can achieve a full calibration of a vector magnetometer without the need of an dedicated maneuver of the magnetometer and the platform on which it is mounted on.

IV. CONCLUSION

This paper investigates magnetic train localization and how unknown magnetometer calibration parameters influence the position accuracy. The investigation is based on two versions of the BCRLB. The first version is derived for the case when the train position and the magnetometer parameters are estimated jointly and the second version is derived for the case when the magnetometer parameters are known. In both bounds, the magnetic field is represented by a GP trained on the basis of real train measurements.

An evaluation and comparison of the bounds showed that the joint estimation of calibration parameters and position only leads to a minor decrease in the achievable position accuracy. In addition, the evaluation suggests that all calibration parameters are observable. Thus, a full calibration of the magnetometer is possible without rotating the sensor around its axes, as it is done in common calibration procedures. Another observation worth mentioning is the increase of the position accuracy for large mean and variance values in the prior distribution of the elements in the calibration matrix. Since the calibration matrix is multiplied with the magnetic field map, large values in the matrix increase the absolute values measured by the sensor and thus increase also the signal-to-noise ratio and thus the position accuracy.

ACKNOWLEDGEMENTS

We want to thank the railway transportation company BRB (”Bayerische Regiobahn”) for their cooperation with the measurement recordings.

REFERENCES

[Bar-Shalom et al., 2001] Bar-Shalom, Y., Li, X. R., and Kirubarajan, T. (2001). *Estimation with Applications To Tracking and Navigation*. John Wiley & Sons, New York.

[Canciani and Raquet, 2017] Canciani, A. and Raquet, J. (2017). Airborne Magnetic Anomaly Navigation. *IEEE Transactions on Aerospace and Electronic Systems*, 53(1):67–80.

[European Environment Agency, 2021] European Environment Agency (2021). *Rail and waterborne – Best for low-carbon motorised transport*. Publications Office.

[Haverinen and Kemppainen, 2009] Haverinen, J. and Kemppainen, A. (2009). Global indoor self-localization based on the ambient magnetic field. *Robotics and Autonomous Systems*, 57(10):1028–1035.

[Kok and Schön, 2016] Kok, M. and Schön, T. B. (2016). Magnetometer Calibration Using Inertial Sensors. *IEEE Sensors Journal*, 16(14):5679–5689.

[Renaudin et al., 2010] Renaudin, V., Afzal, M. H., and Lachapelle, G. (2010). Complete Triaxis Magnetometer Calibration in the Magnetic Domain. *Hindawi Journal of Sensors*, 2010.

[Shockley and Raquet, 2014] Shockley, J. A. and Raquet, J. F. (2014). Navigation of Ground Vehicles Using Magnetic Field Variations. *Navigation*, 61(4):237–252.

[Siebler et al., 2020] Siebler, B., Heirich, O., Sand, S., and Hanebeck, U. D. (2020). Joint Train Localization and Track Identification based on Earth Magnetic Field Distortions. In *2020 IEEE/ION Position, Location and Navigation Symposium (PLANS)*, pages 941–948.

[Siebler et al., 2023a] Siebler, B., Lehner, A., Sand, S., and Hanebeck, U. D. (2023a). Simultaneous localization and calibration (slac) methods for a train-mounted magnetometer. *NAVIGATION: Journal of the Institute of Navigation*, 70(1).

[Siebler et al., 2023b] Siebler, B., Sand, S., and Hanebeck, U. D. (2023b). Bayesian cramér-rao lower bounds for magnetic field-based train localization. In *2023 IEEE/ION Position, Location and Navigation Symposium (PLANS)*, pages 814–820.

[Tichavsky et al., 1998] Tichavsky, P., Muravchik, C., and Nehorai, A. (1998). Posterior Cramer-Rao bounds for discrete-time nonlinear filtering. *IEEE Transactions on Signal Processing*, 46(5):1386–1396.

[Van Trees, 2004] Van Trees, H. L. (2004). *Detection, estimation, and modulation theory, part I: detection, estimation, and linear modulation theory*. John Wiley & Sons.